# Coupling Particle Ordering and Spherulitic Growth for Long-Term Performance of Nanocellulose/Poly(ethylene oxide) Electrolytes

Gleb Bobrov, Stephanie A. Kedzior, Syed Atif Pervez, Aleksandra Govedarica, Gabriele Kloker, Maximilian Fichtner, Vladimir K. Michaelis, Guy M. Bernard, Philipp M. Veelken, Florian Hausen, and Milana Trifkovic*

ABSTRACT: Development of lithium-ion batteries with composite solid polymer electrolytes (CPSEs) has attracted attention due to their higher energy density and improved safety compared to systems utilizing liquid electrolytes. While it is well known that the microstructure of CPSEs affects the ionic conductivity, thermal stability, and mechanical integrity/long-term stability, the bridge between the microscopic and macroscopic scales is still unclear. Herein, we present a systematic investigation of the distribution of TEMPO-oxidized cellulose nanofibrils (t-CNFs) in two different molecular weights of poly(ethylene oxide) (PEO) and its effect on Li^+ ion mobility, bulk conductivity, and long-term stability. For the first time, we link local Li-ion mobility at the nanoscale level to the morphology of CPSEs defined by PEO spherulitic growth in the presence of t-CNF. In a low-MW PEO system, spherulites occupy a

whole volume of the derived CPSE with t-CNF being incorporated in between lamellas, while their nuclei remain particle-free. In a high-MW PEO system, spherulites are scarce and their growth is arrested in a non-equilibrium cubic shape due to the strong t-CNF network surrounding them. Electrochemical strain microscopy and solid-state ^7Li nuclear magnetic resonance spectroscopy confirm that t-CNF does not partake in Li^+ ion transport regardless of its distribution within the polymer matrix. Free-standing CSPE films with low-MW PEO have higher conductivity but lack long-term stability due to the existence of uniformly distributed, particle-free, spherulite nuclei, which have very little resistance to Li dendrite growth. On the other hand, high-MW PEO has lower conductivity but demonstrates a highly stable Li cycling response for more than 1000 h at 0.2 mA/cm² and 65 °C and more than 100 h at 85 °C. The study provides a direct link between the microscopic dynamic, Li-ion transport, bulk mechanical properties and long-term stability of the derived CPSE and, and as such, offers a pathway towards design of robust all-solid-state Li-metal batteries.

KEYWORDS: solid polymer electrolytes, spherulitic growth, Li-ion mobility, lithium dendrites, nanocellulose, sustainable lithium metal batteries
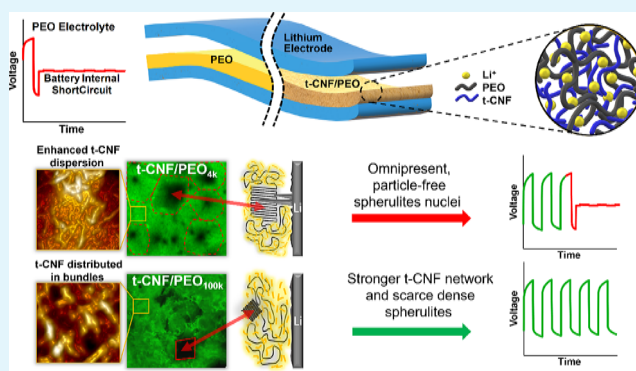
1. INTRODUCTION

Lithium-ion batteries (LIBs) are high-density energy storage devices commonly used for portable electronics and electric vehicles with increasing penetration in other application areas including stationary storage systems.[1,2] Despite their widespread use, commercial LIBs are known to expose users to multiple hazards due to the presence of toxic and flammable organic liquid electrolytes. Another issue is the poor electrochemical stability of lithium within the organic electrolyte, which results in rapid dendrite growth causing fast cell degradation.[3,4] Parallel to the growing interest in overcoming issues in currently utilized batteries, we have seen significant advances in solid-state lithium-ion batteries over the past two decades. Their key advantages are durability, a leak-proof battery cell design, low weights, high energy density, and low reactivity toward the electrodes.[2,5]

With solid electrolyte playing a dual role as both a separator and an electrolyte in a solid-state battery configuration, several criteria such as fast ion transport, a wide electrochemical window, chemical stability, mechanical integrity at ambient and elevated temperatures to suppress lithium (Li) dendrite growth, and the environmental footprint associated with their design must be considered.[6−10] In general, solid electrolytes can be divided into two main subgroups: inorganic solid

electrolytes[11,12] and organic solid electrolytes based on polymers such as poly(ethylene oxide) (PEO), poly(vinylidene fluoride), polyacrylonitrile (PAN), and polyvinyl alcohol (PVA).[6−8] Among the inorganic solid electrolytes, garnet-type electrolytes are widely studied as Li ion conductors due to their high ionic conductivity at 25 °C (up to 10^{-3} S/cm), wide potential window, infinitesimal electronic transport, and electrochemical stability against the Li anode.[11,12] The major flaws of oxide-based solid electrolytes are their rigidity and brittleness, which cause poor mechanical contact with the electrode, resulting in a high interfacial charge transfer resistance.[11−13] In addition, the presence of pores in oxide-based solid electrolytes provide favorable pathways for Li dendrite growth despite their superior mechanical integrity.[14] In comparison, polymer hosts for solid electrolytes such as PEO have several attractive features including a high dielectric constant resulting in strong Li solvating ability, low glass transition temperature of −67 °C ensuring chain mobility in a wide temperature range,[1,15−18] and compatibility with a wide range of solvents. The ethylene oxide units in PEO have a high donor number for Li ions and are spaced at a favorable distance for ion hopping, which are both important characteristics for promoting ion transport.[19,20] However, PEO is a semi-crystalline polymer, and while the amorphous phase with flexible chain segments aids in ion transport,[19,20] it fails to suppress Li dendrite growth, especially in its fully amorphous viscoelastic liquid form at elevated temperatures. In contrast, crystalline PEO regions with slow polymer-chain dynamics obstruct ion transport but contribute to the mechanical strength below melting temperatures.[21,22]

To overcome the challenges associated with polymer-based solid electrolytes, composite solid polymer electrolytes (CSPEs) and cross-linked polymer-based systems present new design opportunities to meet high ionic conductivity and improved mechanical integrity criteria.[5,23−34] For CSPEs, a common approach to improving the polymer electrolyte is the addition of fillers, which can impact both the mechanical and electrochemical properties of the resultant CSPEs.[23,24] Improved conductivity is often realized through the introduction of an ionically conductive filler (e.g., garnet-type ceramics) into the host polymer phase.[24] The utilization of conductive fillers has been shown to increase the room-temperature ionic conductivity of CPSEs by approximately one order of magnitude.[21,24,26,29,30] It was also shown that nonconductive oxide ceramics can influence the electrochemical performance of polymer-based electrolytes.[24] Fillers such as SiO_2, Al_2O_3, and TiO_2 were shown to improve the CSPE ionic conductivity via decreasing the degree of crystallinity of the polymer host and promoting Li salt dissociation via acid−base interactions with either Li cations or anions.[24,31,33,35] Comparing the ionic conductivity values for polymer-based systems with conductive and non-conductive fillers, it can be concluded that both types of fillers show very similar improvements in the ionic conductivity. For cross-linked systems, the polymer network created after oligomer cross-linking is the main contributor to improvements of mechanical integrity and electrochemical performance due to a significant obstruction or even full elimination of polymer crystallization. Another big advantage of this approach is a possibility of its solventless realization. However, for improved conductivity, cross-linked systems still require plasticizers that make them gel-like and not fully dry solid electrolytes. Dry systems do not usually show outstanding ionic conductivity

and stay in a range of 10^{-6} to 10^{-5} S/cm. Regardless of its state, whether it is a dry or a gel electrolyte, reports on long-term cycling and thermal stability of cross-linked systems are scarce.[36,37] Another disadvantage of cross-linked electrolytes is their reduced ability to be shaped and recycled after a cross-linked network is formed.

Recent studies have focused more attention on a relatively new class of fillers in polymer composites. Nanocellulose, particularly cellulose nanofibrils (CNFs) and cellulose nano-crystals (CNCs), which are both ribbon- or rod-like particles composed of cellulose chains held together via hydrogen bonding, show promise as good candidates for reinforcing polymers.[10,38−44] The main advantages of CNFs are their high surface area, high mechanical strength, and ability to form a strong network at low concentrations in water (less than 1%).[43] In addition, there are vast opportunities for surface modification using abundant surface hydroxyl groups.[10] It has been recently reported that 2,2,6,6-tetramethylpiperidine-1-oxyl (TEMPO)-modified CNFs (t-CNF) can contribute to Li salt dissociation and improve PEO-based electrolyte ionic conductivity by preparing CSPEs using a multi-step design consisting of t-CNF aerogel preparation followed by the infusion of PEO-LiTFSI dissolved in acetonitrile into the aerogel and subsequent drying.[42] While a significant improvement in the cycling stability up to 60 °C was achieved in comparison to a neat PEO electrolyte,[40,42] the hypothesis of Li salt dissociation was not proven. Zheng et al. suggested another way of cellulose utilization in a solid-state battery setup.[45] They used it as a separator while it is being sandwiched on both sides with a composite PEO-based solid electrolyte. In that work, $(Er_{0.5}Nb_{0.5})_{0.05}Ti_{0.9}5O_2$ was used as a filler and was proven to have a positive effect on electrolyte dielectric properties. However, the cellulose contribution was limited to improvement of mechanical properties only.

Regardless of the nanofiller utilized, it is evident that the existing literature does not offer clear trends or guidelines on the design of effective CPSEs. Even when studies have investigated similar systems, they often arrive at different conclusions; some reported enhanced conductivity/long-term stability with the addition of nanofillers, and others reported a loss in the performance.[46−53] The microscopic origin of these discrepancies remains unclear.

Our study elucidates that insights into the growth and final morphology of polymeric spherulites intertwined with particle ordering as the effect of that dynamic growth can prove to be a powerful tool to gain predictive capabilities of the CPSE's long-term performance. Using a combination of characterization techniques, including but not limited to laser scanning confocal microscopy (LSCM), electrochemical strain microscopy (ESM),[59] solid-state nuclear magnetic resonance spectroscopy (NMR), and electrochemical studies, we demonstrate the effect of t-CNF on PEO conformation and crystallization patterns. Direct visualization of the micromorphology of the CPSEs via LSCM and polarized light microscopy shows the striking difference in the morphology of the derived CPSE, mainly driven by the dynamic growth of PEO spherulites in the presence of t-CNF. PEO spherulites of low-molecular-weight PEO are evident throughout the volume of the CPSE with t-CNF incorporated within lamellas, while nuclei remain particle-free. On the other hand, high-molecular-weight PEO spherulites are free of t-CNF and their growth is suppressed by a strong particle network in the amorphous phase of PEO. Ultimately, this striking difference in the number and

morphology of spherulites and resulting strength of the t-CNF network was proven to be a main contributor to CSPEs' mechanical integrity and long-term stability during Li stripping and plating experiments. We show that developed CSPEs can be easily molded into thin films (~100 μm) having a room-temperature ionic conductivity of between 10^{-5} and 10^{-4} S/cm and a wide temperature operational window. Cycling studies at 85 °C reveal that the derived CSPEs with high-MW PEO are efficient at suppressing Li dendrite growth at temperatures higher than those for previously reported PEO-based electrolytes. We demonstrate that the synergy of a strong t-CNF network in the amorphous phase and randomly distributed dense spherulites of high-MW PEO is responsible for the enhancement in performance. Electrochemical strain microscopy reveals enhanced mobility of Li^+ in low-MW PEO, while solid-state ^7Li NMR proves that there is no Li^+ coordination with t-CNF. While this study focused on the t-CNF and PEO system, our findings elucidate the importance of linking the spatiotemporal dynamics of spherulitic growth and particle ordering for the effective design of CPSE with enhanced conductivity and long-term performance.

2. EXPERIMENTAL SECTION/METHODS

2.1. Materials. PEO with two molecular weights, that is, 100×10^3 Da (PEO_{100k}) in its powder form and 4×10^3 Da (PEO_{4k}) in the form of pellets, and $LiClO_4$ were acquired from Sigma-Aldrich. t-CNFs produced from wood pulp were purchased from the University of Maine and had a carboxylic acid content of 1.5 mmol/g and dimensions of 10 nm in width and 1–5 μm in length, according to the manufacturer specifications. All water used was purified using a Milli-Q apparatus (18.2 MΩ·cm at 25 °C, pH 6.5) and is referred to as purified or deionized (DI) water in the subsequent text.

2.2. Fabrication of SPEs and CSPEs. Films of PEO-$LiClO_4$ with a [O]:[Li] molar ratio of 10:1 were prepared by solution-mixing in purified water and subsequent film-casting. To produce a homogeneous solution of PEO and $LiClO_4$, the components were dissolved in water and stirred for 48 h at 60 °C in a sealed container using a magnetic stirrer. The solution was then cast into a polystyrene petri dish and left to dry at room temperature for 48 h. Freestanding films with thicknesses of approximately 100 μm were obtained (Figure S1). The films were dried in a vacuum oven at 40 °C for an additional 24 h. Neat t-CNF films were prepared by solution-casting from a 1 wt % aqueous dispersion and dried at ambient temperature for 48 h followed by vacuum-drying at 60 °C for an additional 24 h. CSPEs with 33 and 20 wt % t-CNF in PEO-$LiClO_4$ were prepared by mixing the appropriate amounts of pre-made PEO-$LiClO_4$ solution and 1 wt % t-CNF dispersion for 24 h at 60 °C. The resulting suspension was a highly viscous slurry that was cast in a polystyrene petri dish and kept under mixing for 1 h to remove air bubbles. The casted slurry was dried at ambient temperature for 48 h with subsequent drying in a vacuum for 24 h at 40 °C.

2.3. Morphological Study. Two-dimensional (2D) laser scanning confocal microscopy (LSCM) with a white-light laser source was utilized to characterize the morphology of polymer films containing PEO only, PEO, and Li salt, and the three-component CSPE with PEO, Li salt, and t-CNF. The dried films were placed between two cover slips and imaged with 10×, 20×, and 63× objectives in a 1024 × 1024 resolution with varying pixel sizes achieved depending on the applied magnification. The magnification was chosen based on the characteristic size of the morphological features. To resolve PEO, t-CNF, and Li salt within the films, three techniques were used, namely, polarized transmission, fluorescence, and reflectance imaging, respectively. To unambiguously localize the t-CNF phase within the film and observe its influence on the PEO crystalline domains, the t-CNFs were labeled with the fluorescent dye rhodamine B (Sigma Aldrich) following previously reported protocols and detected using 552 nm excitation light with emissions in the range

of 560–620 nm.[54] Knowing that Li salt can alter the PEO crystallinity even before the introduction of t-CNFs, its localization within the PEO matrix was achieved by reflectance imaging in the region of 638 nm.

In addition to optical LSCM, scanning electron microscopy (SEM) was utilized for a CSPE film surface roughness assessment using a Zeiss Sigma VP SEM at a 2 kV accelerating voltage.

2.4. Thermogravimetric Analysis. TGA was carried out to assess the thermal stability of developed electrolytes. Samples were tested on Netzsch STA 409 PC under a nitrogen atmosphere in a temperature range of 0–500 °C.

2.5. Ionic Conductivity. Electrochemical impedance spectroscopy (EIS) was utilized for ionic conductivity measurements. The cell assembly consisted of the CSPE film sandwiched between two blocking stainless steel electrodes connected to the potentiostat clamps with copper tape as a current collector. For neat t-CNF samples, gold sputtering was used to create an analog of electrodes on both sides of the film and copper tape was attached to the gold coating for the EIS measurements. All samples were tested in a temperature range of 25–100 °C and a frequency range between 0.1 Hz and 3 MHz using a DC potential value of 20 mV. The x-axis intercepts of the suppressed semicircles on the resulting Nyquist plots were used as the resistance value of the samples (Figure S2). The resultant ionic conductivity of the tested sample was calculated using the formula:

$$\sigma = L/(A \times R) \tag{1}$$

where σ is the sample conductivity (S/cm), L represents the CSPE film thickness (cm), A is the contact area between the electrode and electrolyte (cm^2), and R is the sample resistance (Ω) obtained from the Nyquist plot.[6]

2.6. Cycling Behavior. Chronopotentiometry (CP) was carried out to observe the lithium stripping/plating response of the CSPEs. Instead of the stainless-steel blocking electrodes, the CSPE was sandwiched between lithium electrodes in a symmetric cell configuration under an argon environment in a glovebox. Depending on the sample cycling response, different current densities from 0.025 to 0.5 mA/cm^2 and temperatures of 65 and 85 °C were used. For samples successfully passing 50 and 100 h tests at the given current density and temperature, both the current and temperature were increased for further testing.

2.7. Crystallization Behavior. The degree of crystallinity and melting temperatures were obtained via differential scanning calorimetry (DSC) measurements on a DSC 3 Star system (Mettler Toledo) in a temperature range from 0 to 100 °C with cooling and heating rates of 2 °C/min. The degree of crystallinity was normalized to the PEO content in each sample.

2.8. Flexibility and Tensile Testing. To ensure film flexibility, a qualitative bending test was conducted on each sample.[40] Samples were folded at 180 °C at room temperature and after being heated up to 100 °C. They were kept folded for 1 min and then released (Figure S1). The flexibility of the films was characterized based on whether they showed any visible signs of cracking in the folding area or not. Samples without significant cracks that restored their initial shape after bending were considered flexible.

2.9. Rheological Measurements. A stress-controlled rotational rheometer (Anton Paar MCR-302) with a cone and plate geometry (25 mm in diameter and a gap size of 1 mm) was utilized to conduct the rheological measurements. The oscillatory amplitude sweep experiments were performed on PEO solutions and t-CNF dispersions in water and PEO water solutions at a frequency of 0.1 Hz in a strain.

2.10. Solid-State Nuclear Magnetic Resonance Spectroscopy. Solid-state ^7Li NMR data were acquired using an Avance III HD 400 NMR spectrometer. Solid-state NMR spectra were acquired using a 4 mm double resonance (H/X) Bruker probe tuned to ^7Li (ν_L = 155.6 MHz). Samples were packed into 4 mm (outer diameter) zirconia rotors and sealed using a Kel-F drive cap. Solid-state NMR spectra were acquired using a Bloch pulse (ν_{rf} = 62.5 kHz) with 10 s recycle delays. Thirty-two to 1200 transients were co-added for these

spectra with more scans for the cycled samples due to limited samples. NMR spectra were acquired under both non-spinning conditions or with magic-angle spinning (MAS) at a spinning frequency of 5 kHz. All ^{7}Li NMR spectra were referenced using 1 M LiCl solution (0.0 ppm) and acquired at room temperature.

2.11. Electrochemical Strain Microscopy. A Bruker Dimension Icon (Bruker, Santa Barbara, CA, USA) atomic force microscope (AFM) operating in an argon-filled glovebox was utilized for AFM image acquisition and electrochemical strain microscopy (ESM) measurements. The AFM tip radius of the curvature is less than 20 nm. Based on the tip size, the lateral resolution is approximately 25−30 nm. To ensure a stable tip−sample interaction, a slow scanning speed of approximately 0.2 Hz was applied. ESM is a special mode of contact AFM that allows us to probe local variations of ion mobility at the nanoscale and compare them with different materials.[58] During ESM, an alternating current (AC) is applied on a cantilever tip and always matched the contact resonance frequency of the cantilever. The contact resonance frequency (CRF) and amplitude were tracked and recorded with a phase-locked loop (HF2LI, Zurich Instruments, Zurich, Switzerland).[59] A higher ESM signal amplitude usually refers to a higher local mobility of ions in the material. All images depicting an ESM amplitude signal and sample topography were recorded simultaneously. For measurements, a cantilever with a free resonance peak around 75 kHz and a conductive platinum iridium coating (PPP-EFM, nominal spring constant of 2.8 N/m, Nano World AG, Neuchatel, Switzerland) was utilized.

3. RESULTS AND DISCUSSION

PEO crystallinity has been shown to have a significant impact on the ionic conductivity and hence the performance of CSPEs.[7,47,55] We investigated changes in the PEO crystallization behavior as well as the surface and bulk morphology of PEO films with two different molecular weights (PEO_{4k} and PEO_{100k}) upon the addition of $LiClO_4$ and t-CNFs. The two different chain lengths were chosen in order to probe the effect of crystallinity without sacrificing the chain segmental motion of the two PEO candidates. PEO_{4k} is approximately the entanglement molecular weight for PEO and is therefore expected to have high chain mobility as well as a high fold length, while PEO_{100k} was previously reported to have approximately the same ionic conductivity as PEO_{4k}.[16,17,56] DSC results in Figure 1a,b reveal that the addition of $LiClO_4$ decreased the degree of crystallinity for both PEO_{4k} and PEO_{100k}, while the introduction of t-CNFs influenced the crystallinity and crystallization behavior more drastically. The films containing t-CNFs are characterized by the significant decrease in overall crystallinity, a wider melting region, and a shift of the onset of melting and crystallization toward lower

temperatures (Figure 1b). This effect becomes more prominent with the increase in t-CNF content from 20 to 33 wt % and decrease in the PEO molecular weight from 100 to 4 kDa. As the PEO semi-crystalline nature at ambient temperature is one of the reasons for its poor ionic conductivity, such a crystallization retardation effect induced by t-CNF after proper optimization can be a pathway toward PEO composites with improved ambient temperature ionic conductivity.[57] Since both PEO chains are hydroxyl-ended, the larger drop in the crystallinity of PEO_{4k} in the presence of t-CNFs could be attributed to the enhanced interaction in the PEO solution/t-CNF suspension prior to film formation between carboxyl groups on the t-CNFs and a larger number of hydroxyl groups present on the PEO_{4k} chains. Alternatively, the lower viscosity of the PEO_{4k} solution could lead to a better t-CNF network distribution in the PEO_{4k} system prior to film-casting and consequently provide a better hindrance for crystalline spherulite growth during the drying step.

The thermal stability of the neat PEO electrolyte and composite film was studied by thermogravimetric analysis (TGA). Results show that both electrolytes are relatively stable up to 400 °C. The slight degradation observed between 250 and 370 °C in the PEO/t-CNF composites is attributed to the decomposition of carboxyl groups on the t-CNF and is in agreement with previous reports.[42] In addition, the absence of a significant mass loss around 100 °C allows us to make a conclusion that all the water was removed from films during the drying procedure (Figure 2).
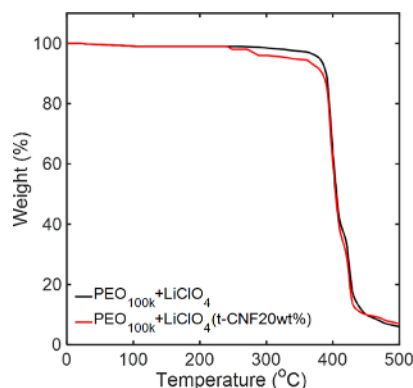

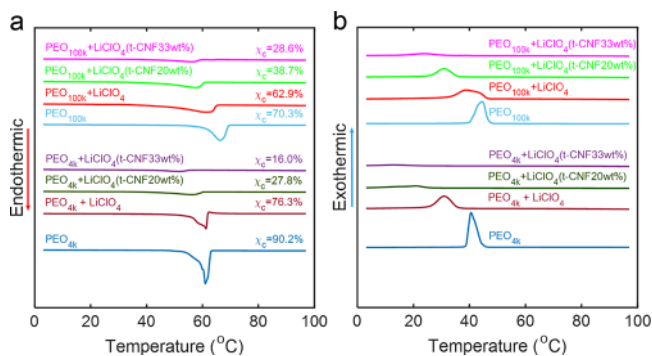**Figure 2.** TGA curves of the PEO electrolyte and PEO/t-CNF composite.

A combination of SEM and LSCM imaging allowed for probing the differences between the CSPE surface and bulk morphology at an unprecedented level of detail and provided deeper insights into the origin of crystallinity changes that we observed in the DSC curves. Figure 3 shows a comprehensive morphological analysis of both CPSE systems (PEO_{4k} and PEO_{100k}) with 20 wt % t-CNFs. Figure 3a,b shows SEM images of pure PEO_{100k} and PEO_{100k} with $LiClO_4$ indicating spherulitic formations on their surface, while Figure 3e−h shows the spherulites in bulk through the reflectance and polarization modes.

As seen from all SEM and reflection/polarization images, the addition of $LiClO_4$ results in the formation of spherulites with depressed edges and a reduction of their overall size. It is noticeable that the PEO spherulites are tightly packed and occupy all visible areas in both pure PEO and PEO with $LiClO_4$. However, the reflectance mode of LSCM allows us to
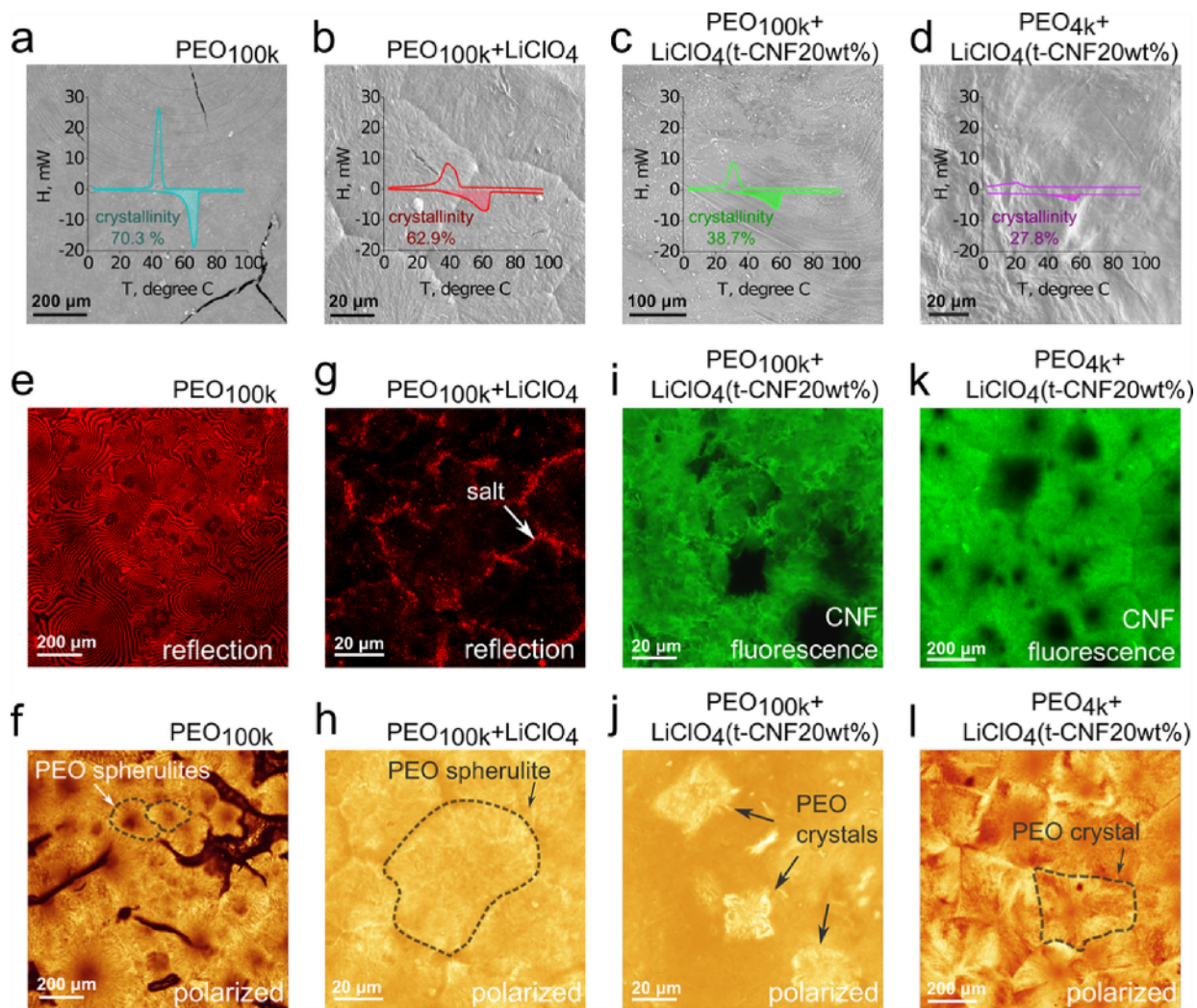

Figure 1. DSC scans of pure PEO with different MWs, PEO + $LiClO_4$ electrolytes, and CPSEs with $LiClO_4$ and t-CNFs during (a) heating and (b) cooling.

Figure 3. Morphological and crystallinity characterization of pure PEO, PEO + LiClO$_4$, and CSPE samples with a t-CNF content of 20 wt %. (a–d) SEM of pure PEO, PEO + LiClO$_4$, PEO$_{100k}$-based CSPE, and PEO$_{4k}$-based CSPE with their respective DSC curves and crystallinity values overlaid. (e–l) Combination of polarized transmission, reflection, and fluorescent microscopy of the four samples.

observe aggregation of LiClO$_4$ at the edges of the growing crystals (red-labeled regions, Figure 3g). A similar observation was previously made through a combination of X-ray diffraction and polarized microscopy techniques in a mixture of high-molecular-weight PEO (5 × 10^6 Da) and LiTFSI.[55] While the addition of LiClO$_4$ affects the PEO crystal size and melting behavior, it does not drastically change the degree of crystallinity, as evident from the overlaid DSC curves in Figure 3a,b.

With the addition of t-CNFs, drastic changes are evoked in both the film morphology and crystallinity of the PEO$_{100k}$-based CSPE (Figure 3c,i,j). The SEM image shown in Figure 3c suggests a smooth surface with no appearance of PEO$_{100k}$ spherulites. However, irregularly shaped, isolated PEO crystals surrounded by the extensive t-CNF network within the amorphous PEO were observed within the bulk of the CPSE (Figure 3i,j). It is important to note that the CNF network fluorescence does not overlap with PEO crystalline regions, suggesting that the suppression of crystal growth is imparted by the strong fiber network that surrounds the nuclei at the beginning of crystal growth. The addition of t-CNFs eliminates the appearance of LiClO$_4$ aggregates under the reflectance mode (Figure S3). The disappearance of LiClO$_4$ aggregates

could be attributed to either enhanced Li salt dissociation in the presence of t-CNF or the fact that a decrease in PEO crystallinity allows easier LiClO$_4$ solvation in the increased volume of the amorphous PEO phase.[40] It is important to note that, with an LSCM resolution limit of ~200 nm, individual t-CNFs are not resolvable. However, the t-CNF network formation is only evident through fluorescent imaging (Figure 3i), while SEM provides no information on the distribution of t-CNF (Figure 3c). The morphological changes observed with the addition of t-CNFs to the CSPE based on PEO$_{100k}$ are in agreement with the decrease in the degree of crystallinity (Figure 1a,c).

PEO$_{4k}$-based CSPE morphological changes are significantly different than those of the PEO$_{100k}$-based CSPE. While DSC results showed that the decrease in crystallinity (Figure 3d) was more significant in the PEO$_{4k}$-based CSPE, polarization microscopy reveals uniformly distributed, crystalline-like domains (Figure 3l). Note that the fold length of PEO$_{4k}$ spherulites is significantly higher than that of PEO$_{100k}$ (Figure S4), resulting in spherulites visible to the naked eye (~1 mm in diameter) when t-CNF is not present in the system. A closer inspection of the CNF fluorescence signal and PEO$_{4k}$ crystalline regions (Figure 3k,l) indicates that, with the
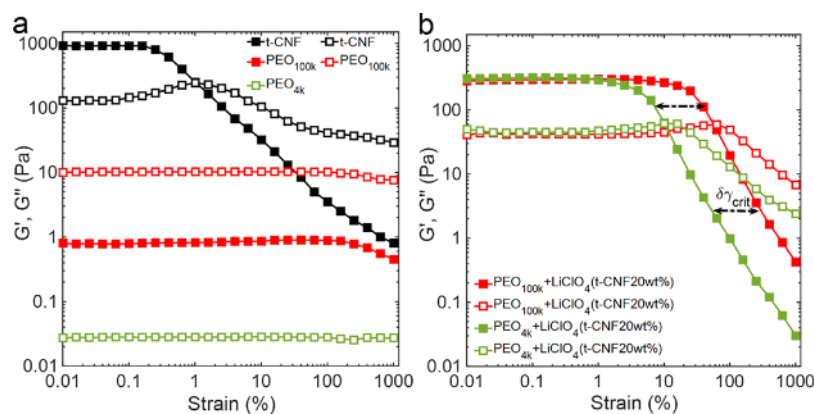
Figure 4. Storage ●′ (filled symbols) and loss ●″ (unfilled symbols) modulus versus strain sweep of (a) PEO solutions and t-CNF dispersion in water and (b) CSPE dispersion in water.

exception of spherulite centers (dark regions in Figure 3k), t-CNF are uniformly distributed within spherulites and oriented in the direction of their growth. The morphological investigation suggests that the nuclei of spherulites are tightly packed with PEO_{4k} chains, while their further growth allows for the incorporation of t-CNFs within the spherulites' periphery. The decrease in the degree of crystallinity measured by DSC confirms that the spherulites are of "low quality" and have amorphous regions enclosed between their widely spaced crystalline lamellas. These differences in the mechanism of crystallinity suppression in PEO with varying chain lengths are significant as the structural features of electrolytes directly affect their performance in terms of conductivity and long-term stability.

Another consequence of differences in the suppression of crystal growth is that t-CNFs are better dispersed in PEO_{4k} (as seen by a uniform field of fluorescence in Figure 3k) compared to t-CNF bundles observed in PEO_{100k} (Figure 3i). This difference in the extent of t-CNF dispersion could be thermodynamically or kinetically driven. In the PEO_{4k} system, due to the higher number of hydroxyl terminal groups on the PEO_{4k} chains, there are approximately 20 times more sites for hydrogen bonding between PEO_{4k} and t-CNF in comparison to the PEO_{100k} system. At the same time, the PEO_{100k} solution has significantly higher viscosity, which could hinder t-CNF dispersion. To investigate this further, we probed the viscoelastic properties of pure PEO solutions and the changes that result from the introduction of $LiClO_4$ and t-CNF. As expected, due to the difference in the polymer chain length, the t-CNF/PEO_{4k} solution has a much lower storage (●′) and loss (●″) modulus (with ●′ below the rheometer's detection limit) than the PEO_{100k} solution. However, upon the addition of t-CNFs and $LiClO_4$, both dispersions have similar ●′ and ●″ in their linear viscoelastic region (●′ and ●″ are independent of the applied strain). The difference in the relative increase of ●′ and ●″ in the two systems indicates that the kinetic effect is likely dominant as the increased number of hydrogen bonds alone would not be sufficient to produce this rheological response. Further insights into the modulation of rheological properties arising from the introduction of t-CNFs can be gained by comparing the critical strain between the two systems. As seen from Figure 4, the critical strain for the PEO_{100k} + $LiClO_4$ (t-CNF 20 wt %) system is almost one order of magnitude larger. The above results suggest that there is an interplay between the extent of t-CNF dispersion and the

resulting network strength. The enhanced dispersion of t-CNF in the PEO_{4k} system leads to the equivalently strong network at rest in the PEO_{4k} system. However, the addition of t-CNF to the PEO_{100k} system results in a more bundled network of t-CNF and entangled PEO_{100k} chains with a larger relaxation time, which consequently leads to a higher resistance to strain.[56]

Figure 5 depicts the ionic conductivity of the CSPEs with different PEO MWs as a function of temperature during
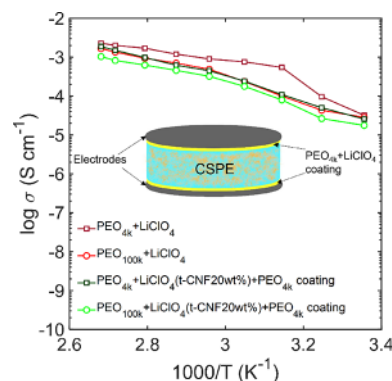

Figure 5. Arrhenius plot of ionic conductivity for samples PEO + $LiClO_4$ and CSPEs with 20 wt % t-CNF loading coated with an additional highly conductive slurry of PEO_{4k} + $LiClO_4$.

cooling cycles. The ionic conductivity response to temperature change suggests an Arrhenius behavior of the electrolyte conductivity in a temperature range from 25 to 100 °C. In the temperature range below the melting point of PEO, all tested CSPEs exhibit significantly lower ionic conductivity than pure PEO + $LiClO_4$ samples. The t-CNF/PEO_{100k}-based CSPE with the highest t-CNF loading of 33 wt % exhibits the lowest ionic conductivity among all the tested electrolytes (Figure S5). Compared to PEO, neat t-CNF has a significantly lower ionic conductivity of 5.5×10^{-8} S/cm and increasing the content of the low-ionically conductive t-CNF effectively decreases the amount of PEO in the resulting film. As a result, the amount of hopping sites for Li ions at higher t-CNF loadings is significantly decreased while the ion hopping distance is increased within the PEO matrix, inevitably leading to a higher activation energy needed for Li ion transport.[20] Increasing both the MW of PEO and the t-CNF content causes more steric entanglement, hence reducing the mobility of the PEO
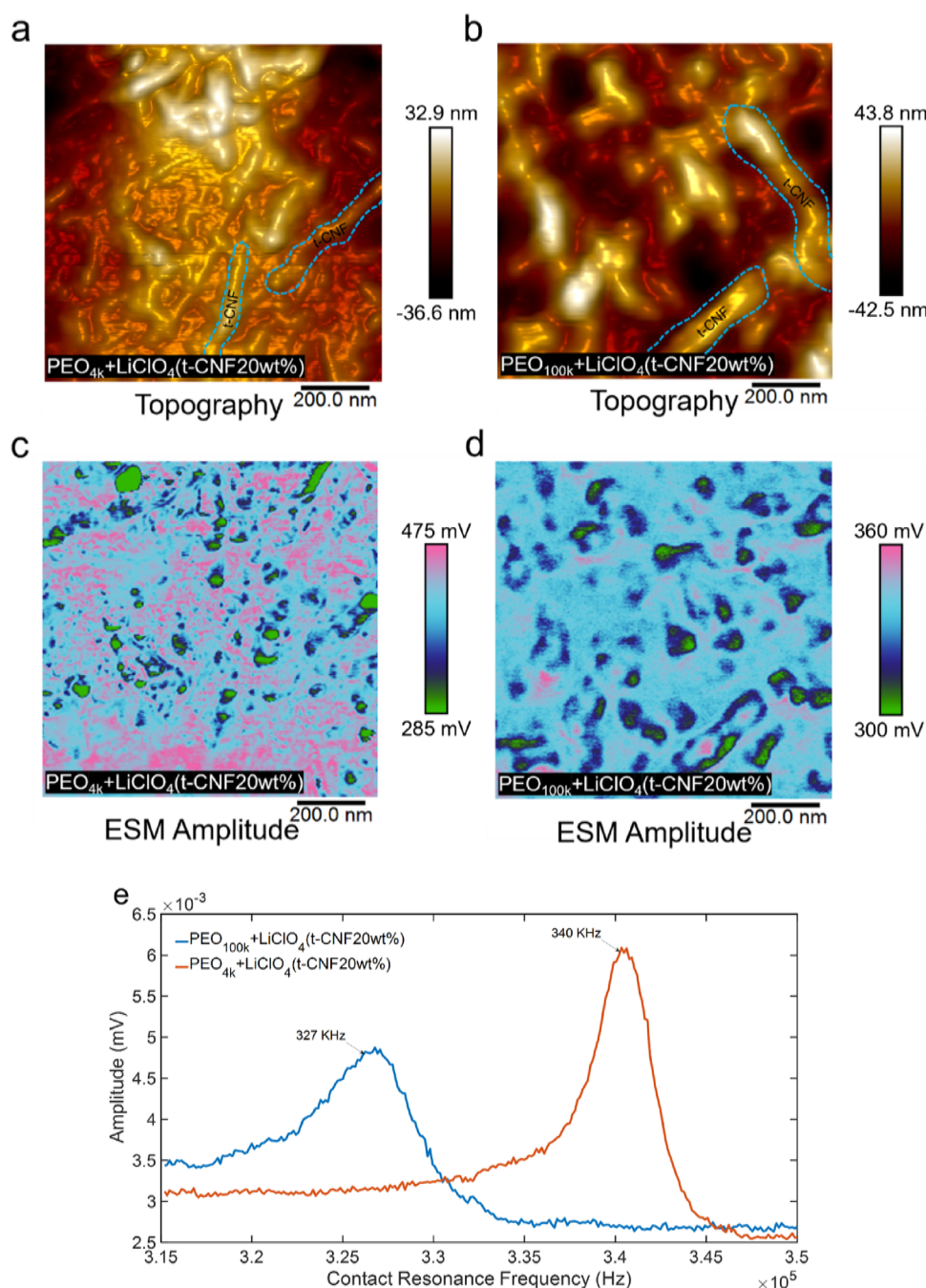
Figure 6. (a, b) CSPE topography, (c, d) ESM signal amplitude, and (e) contact resonance frequency.

chains that ultimately affects ion hopping. In addition, CSPEs' surface roughness and the consequent electrolyte−electrode contact area can influence the conductivity results.

The difference in the crystallinity of PEO_{4k} and PEO_{100k} (Figure 1a) impacts the CSPE behavior during EIS measurements and the Arrhenius plot configuration in an expected manner. CSPE samples exhibit different ionic conductivity values during heating and cooling cycles (Figure S6) with an order of magnitude higher ionic conductivity during cooling. The fact that this difference is more noticeable for the PEO_{100k}-based CSPE, especially at lower temperatures, while it almost disappears above the PEO melting temperature implies that the observed discrepancy is mostly due to the poor electrode−electrolyte contact. At room temperature, the contact

resistance between the stiff CSPE and the electrode is high, while PEO softens with increasing the temperature providing a better contact and hence reducing the contact resistance.

The challenge of the poor electrolyte−electrode contact was overcome through incorporation of the PEO_{4k} + $LiClO_4$ slurry casted on both sides of the PEO_{4k} and PEO_{100k}-based CSPEs. The ionic conductivity of the coated CSPE samples at ambient temperature was up to three orders of magnitude higher than one of CSPE samples without the slurry coating within the EIS cell (Figure S5). The bulk ionic conductivity (Figure 5) of the CSPE is at the level of neat PEO even with 20 wt % t-CNF, indicating that the suppression of PEO crystallinity with the addition of t-CNFs offsets the lower content of PEO. The calculated weight percentages of the amorphous PEO phase
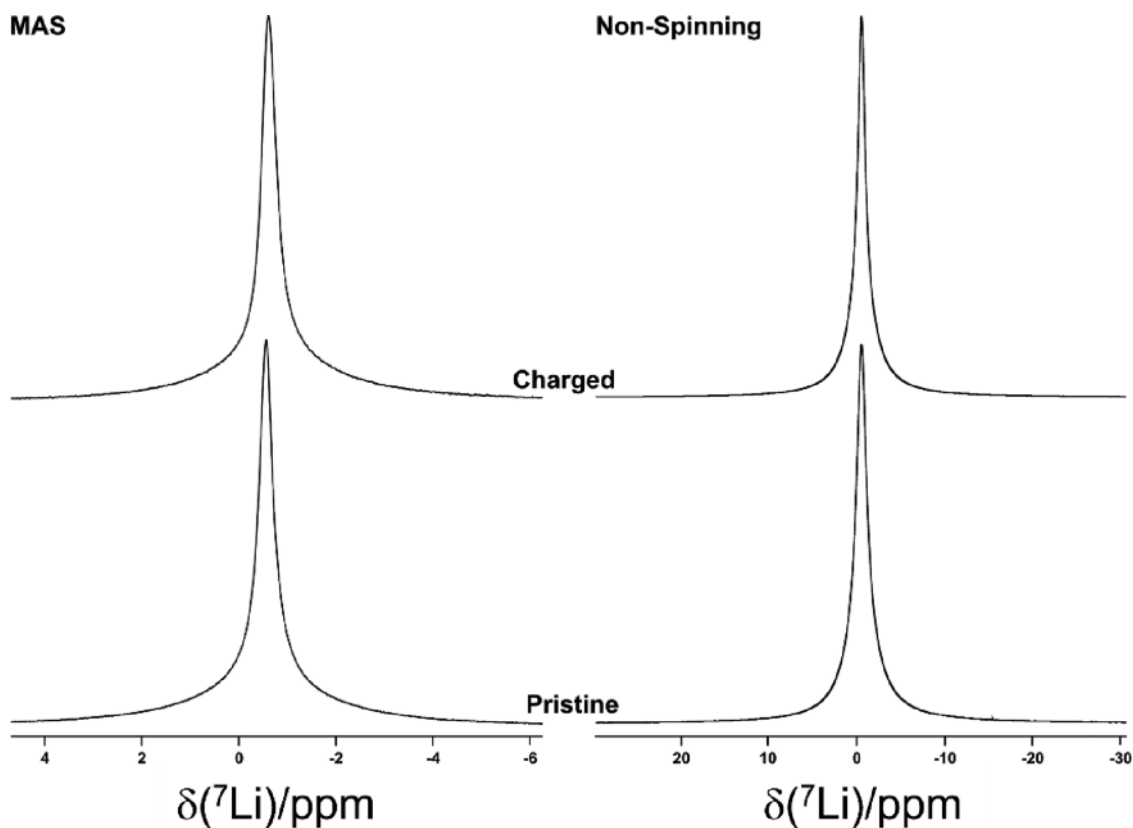
Figure 7. ^{7}Li NMR spectra for MAS (left, 5 kHz) and non-spinning (right) samples acquired before (lower traces) and after (upper traces) chronopotentiometry. Spectra were acquired at 9.4 T (155.6 MHz).

based on the DSC results in $PEO_{100k}/LiClO_4$ and $PEO_{100k}/LiClO_4$ (t-CNF 20 wt %) samples are 50 and 52 wt %, respectively. Therefore, the growth suppression of large and highly ordered spherulitic formations helped counterbalance the inherent low ionic conductivity of t-CNFs while improving the mechanical integrity of the CSPEs. The CSPE samples stay intact in a wide temperature range from 25 to 120 °C, while pure PEO films lose their stiffness and shape above 50 °C regardless of the PEO MW (Figure S7).

Electrochemical strain microscopy (ESM) measurements were conducted to understand the difference in mobility of Li^+ ions in the two systems. Under the influence of the electrical field at the cantilever tip, lithium ions inside the material move toward or away from the tip. Schön et al.[58] demonstrated that there is a link between the ionic conductivity, local ion mobility, and tip−sample interaction. Therefore, for ceramic materials with an inherently higher ionic conductivity, both the contact resonance frequency (CRF) of the cantilever and amplitude of ESM signal are higher compared to ones recorded for polymer-based electrolytes.[59] As a cross-talk between the sample topography and ESM signal has been proven to be an important factor in data interpretation, the first step for us was to prove that our ESM results are not affected by the CSPE topography. Figure S8 depicts the PEO_{100k} + $LiClO_4$ (t-CNF 20 wt %) sample topography and its corresponding ESM amplitude signal, and the results demonstrate that there is no direct correlation with the ESM amplitude and sample roughness. In addition, the frequency phase shift was recorded as an indicator of different phases in the composite. Since this depends on the mechanical properties of the material, the presence of at least two contrast phases in Figure S9 serves as

supporting evidence that we can distinguish different composite components for further interpretation.

CSPEs based on PEO with different MWs were analyzed, and both the contact resonance frequency (CRF) and ESM amplitude signal are demonstrated in Figure 6. The higher ESM signal amplitude and more pronounced CRF peak (Figure 6e) observed for PEO_{4k} + $LiClO_4$ (t-CNF 20 wt %) demonstrate a higher ionic conductivity and a higher ionic mobility, respectively.[58,59] Higher mobility of Li ions in the PEO_{4k} system is expected due to the enhanced segmental motion of shorter PEO chains and poorly organized spherulitic structures (observed by LSCM). Both PEO systems with a lower ESM signal amplitude have distinctive fiber-shape features (Figure 6a,b). However, these features have a larger diameter in the PEO_{100k} system, elucidating that they are t-CNF bundles, which is further supported by the presence of t-CNF bundles in LSCM images and higher resistance to strain in the PEO_{100k} system.

Solid-state ^{7}Li NMR spectroscopy was performed to determine whether the t-CNF plays any role in Li^+ ion transfer or its contribution to the electrolyte performance is mainly based on the morphological reorganization of polymer chains. The solid-state ^{7}Li NMR spectra for the PEO_{100k}-based composite electrolyte were examined before and after chronopotentiometry (Figure 7). As can be seen from ^{7}Li MAS NMR spectra, in both cases, a virtually identical single resonance (δ_{iso} = −0.6 ppm and FWHM = 0.4 ppm) is observed. This resonance is associated with Li ions distributed in PEO as $LiClO_4$ as reported previously,[57] while no evidence of dendritic formation post-charging was found. The NMR data for the non-spinning samples further support the
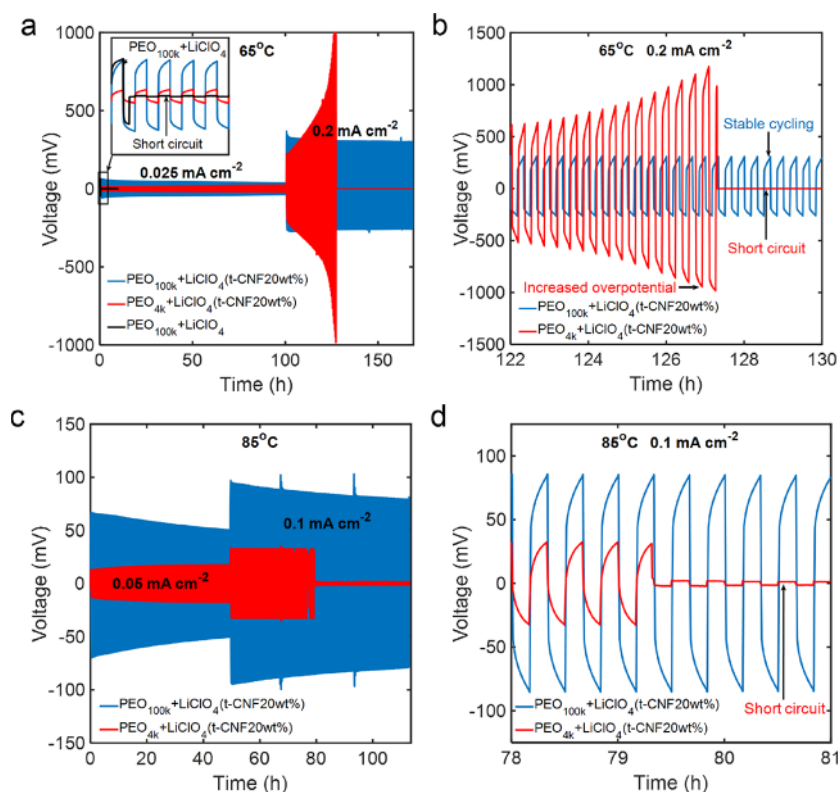
Figure 8. Chronopotentiometry of the lithium plating and stripping in a symmetric cell. (a) Cycling at 65 °C for films with and without CNF containing PEO of different molecular weights: PEO_{100k} - black, CSPE based on PEO_{4k} - red, and PEO_{100k} - blue. (b) Inset of the voltage profile showing the increased overpotential for the PEO_{4k}-based sample (red) and its subsequent short-circuiting. (c) CSPE cycling at 85 °C. (d) Inset of the voltage profile showing the PEO_{4k}-based sample (red) short-circuiting after 79 h of operation.

conclusion that the t-CNF does not change the local Li ion chemical environment (line width of ~1 ppm for non-spinning samples) since both the chemical shift and line width would be sensitive to the ion location and dynamics (for example, upon $LiClO_4$ dissociation or Li ion conduction), supporting a rather freely mobile Li ion at room temperature. These findings support our hypothesis that any changes in Li ion transfer can be attributed to microstructural change (inherent difference in the segmental motion of PEO with different chain lengths and alteration of spherulitic growth by the presence of t-CNF).

Chronopotentiomety (CP) experiments were carried out on the PEO_{100k} electrolyte (as a control), PEO_{100k} + $LiClO_4$ (t-CNF 20 wt %), and PEO_{4k} + $LiClO_4$ (t-CNF 20 wt %) to obtain the Li stripping/plating voltage profiles for the Li symmetrical cells as shown in Figure 5a. Electrolytes without t-CNF could not withstand cycling at 65 °C, which is mainly caused by the complete melting of PEO_{100k}, which led to the loss of mechanical integrity and the immediate short-circuiting through the liquid-like polymer phase thereafter (Figure 8a). The addition of t-CNFs resulted in a significant improvement in long-term stability. At 65 °C, CSPE samples containing both low and high-MW PEO were able to withstand prolonged cycling at a current density of 0.05 mA/cm². This can be attributed to the significant physical reinforcement of the PEO phase by the t-CNF network. However, after increasing the current density to 0.2 mA/cm² in a cell with PEO_{4k}-based CSPEs, the overpotential started increasing and shortly reached very high values (Figure 8a,b). Only the PEO_{100k}-based CSPE showed a highly stable cycling behavior for more than 150 h regardless of the current density applied. We attribute the high stability to the synergistic effect of the

isolated tight spherulitic structures obtained with longer polymer chains and the presence of the strong t-CNF network derived from bundles of fibers resisting the Li dendrite growth (Figure 3j). In contrast, the PEO_{4k}-based CSPE microstructure showed a more uniform t-CNF distribution, which spanned larger but looser spherulitic structures. Consequently, its mechanical robustness against the Li dendrite growth was lower, which led to short-circuiting. The above results are consistent with the viscoelastic properties presented earlier, which indicated higher resistance to strain of the PEO_{100k} system. At the beginning of dendrite growth, the three-dimensional t-CNF network persists in both systems. Due to the stress imposed by growing Li dendrites, the breakdown of the structure begins with the formation of micro cracks in CPSEs. As the strain increases, a macro crack finally can rupture through the sample. In the PEO_{100k} system, the combination of the strong t-CNF bundle network and high entanglement of PEO chains (longer relaxation times) synergistically contribute to the enhanced resistance to dendrite growth and enhance the long-term stability.

The cycling behavior of CSPEs in the temperature region beyond the melting point of PEO has not been investigated previously. To accurately assess the t-CNF network contribution to the Li dendrite suppression within the CSPEs, Li stripping/plating tests were carried out at 85 °C. In Figure 8c, CP results demonstrate the high stability of the PEO_{100k} + $LiClO_4$ (t-CNF 20 wt %) CSPE. Regardless of the current density, the electrolyte exhibited a stable overpotential, while the PEO_{4k}-based sample experienced a short circuit at 0.1 mA/cm² (Figure 8c,d). The DSC results (Figure 1a) confirmed that, at 85 °C, PEO_{100k} is completely melted, indicating that

the t-CNF network is the main contributor to the CSPE mechanical integrity and dendrite growth suppression at this temperature. The strong t-CNF bundles along with randomly distributed t-CNF-free regions provide sufficient resistance to dendrite growth. These findings demonstrate that the morphology of the spherulites and distribution of nanofillers within the CPSE matters equally for conductivity and long-term stability.

To assess the long-term stability of the PEO_{100k}/t-CNF electrolyte, we performed 600+ cycles at 65 °C at various current densities.

The developed composite electrolyte with 20 wt % t-CNF performed well not only at being widely used for a CP current density of 0.2 mA/cm^2 (Figure 9a) but also at increased current densities of 0.35 and 0.5 mA/cm^2 (Figure 9b), which confirms the contribution of the t-CNF network to the lithium dendrite growth suppression.
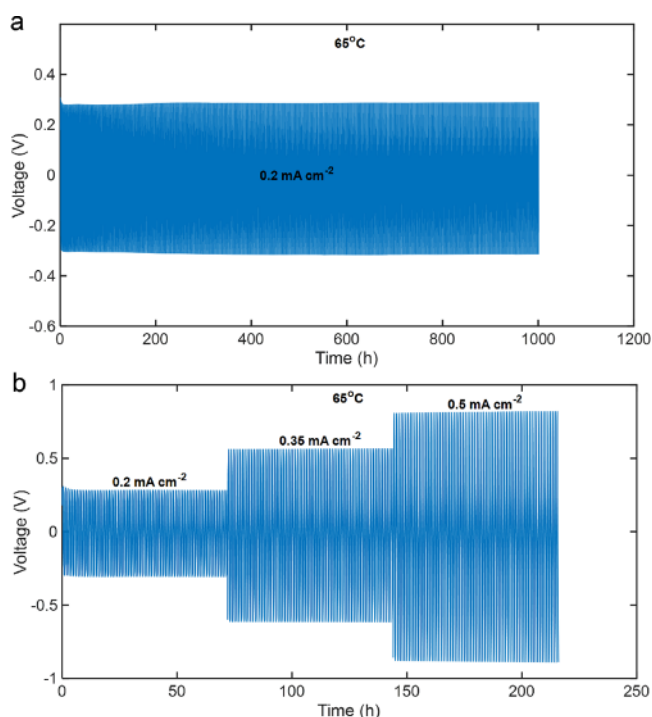

Figure 9. Chronopotentiometry of the lithium plating and stripping in the PEO_{100k}/t-CNF based composite electrolyte in a symmetric Li cell. (a) Long-term performance and (b) performance at different current densities.

Room-temperature performance of the developed CSPEs, as expected, scales with the electrolyte conductivity (Figure S10).

Post-mortem SEM was utilized to examine the developed electrolytes for signs of dendrite formation during CP experiments. CSPEs were studied before and after CP was performed in a Li symmetric cell. While the film based on PEO_{100k} demonstrates a rougher surface due to t-CNF agglomeration and has darker spots that originated from morphology imperfections before cycling (Figure 10b), it can clearly be seen that a much smoother neat PEO_{4k}-based film develops dark features of 1−10 microns in size after CP (Figure 10c and Figure S11). On the other hand, the PEO_{100k}-based CSPE does not depict any new features after CP (Figure 10d and Figure S11), which supports the assumption of its higher resistance to lithium dendrite formation and growth.
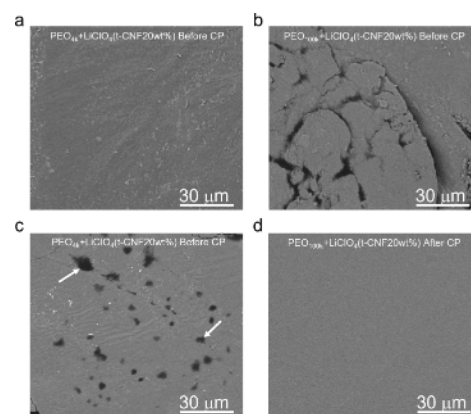

Figure 10. SEM images of the CSPE surface (a, b) before and (c, d) after CP at room temperature and 0.2 mA/cm^2.

Both electrolytes became smoother after cycling, which makes new morphological features more noticeable. The acquired results correlate with earlier reported patterns intrinsic to SEM imaging of lithium dendrite growth in solid-state electrolytes; appearance of new darker regions on the surface of LLZO-based electrolytes observed after cycling are generally attributed to the formations consisting of chemical elements with lower atomic numbers compared to brighter surrounding—in our case, lithium.[60,61]

It is also important to note that our EIS and CP results show that fabrication of CSPE in an aqueous environment has comparable ionic conductivity and cycling stability of Li-based electrolytes produced with toxic solvents such as acetonitrile and dimethyl sulfoxide. The proposed fabrication method therefore meets the previously reported CSPE performance while improving on the overall environmental impact of our developed materials.

4. CONCLUSIONS

Using a multi-scale characterization approach through the combination of solid-state NMR, ESM, in situ microstructural analysis, and bulk rheological and electrochemical characterization, we have studied the effect of t-CNF-PEO interactions on the CSPE morphology, PEO crystallization dynamics, and its influence on conductivity and long-term stability of the derived CPSEs. Our findings demonstrate that reduction in bulk crystallinity, commonly taken as the indicator of particle suitability for a CPSE system, can be often deceiving. By investigating PEO with two different molecular weights, for the first time, we have shown that there is a delicate balance between the extent of interaction of PEO chains and t-CNFs and the viscosity of the PEO solution, which ultimately governs particle ordering within or outside of spherulites in the derived CPSE. t-CNFs are not only able to form a continuous entangled network contributing to the mechanical integrity of the CSPE but also able to induce morphological changes to the PEO spherulite structure, affecting the electrochemical performance. The enhanced dispersion of t-CNF and its incorporation in PEO_{4k} spherulites suppresses the overall crystallinity without a significant loss in ion conductivity of the derived CPSE. However, well-dispersed t-CNFs do not result in a strong network necessary to entirely suppress dendrite growth during Li stripping/plating experiments due to the presence of particle-free, uniformly distributed nuclei of PEO_{4K} spherulites. The PEO_{100k} system demonstrates an excellent

electrochemical response with a stable Li stripping/platting behavior for over 1000 h when tested at elevated temperatures (65 °C) at the cost of a slight decrease in room-temperature conductivity. Moreover, developed CSPEs demonstrate less temperature dependence of their ionic conductivity due to the t-CNF retardation effect on the PEO crystallization process—the PEO phase can stay mainly amorphous even at 30 °C. For the first time, we link local Li-ion mobility at the nanoscale level with ESM to the microstructural features depicting spherulite morphology (via polarized microscopy) along with particle distribution (via confocal microscopy), which are not detectable with a commonly utilized SEM technique. We finally link these two scales to the bulk performance via long-term stripping/plating experiments. Successful implementation of the ESM technique with a developed CSPE and coherence of current results with past studies prove its consistency for the purpose of probing the local ionic conductivity in hybrid materials on a nanoscopic scale. Since t-CNFs can be modified to carry diverse surface functional groups, which in turn can have added benefits on the CSPE performance, further investigation and optimization is needed to understand the full potential of cellulosic nanomaterials for lithium-metal-based solid-state batteries.

■ AUTHOR INFORMATION

Corresponding Author

Milana Trifkovic − *Department of Chemical and Petroleum Engineering, University of Calgary, Calgary, AB T2N 1N4, Canada;* ◉ orcid.org/0000-0002-3954-2777; Email: mtrifkov@ucalgary.ca

Authors

Gleb Bobrov − *Department of Chemical and Petroleum Engineering, University of Calgary, Calgary, AB T2N 1N4, Canada;* ◉ orcid.org/0000-0002-9825-1734

Stephanie A. Kedzior − *Department of Chemical and Petroleum Engineering, University of Calgary, Calgary, AB T2N 1N4, Canada;* ◉ orcid.org/0000-0003-3112-3890

Syed Atif Pervez − *Helmholtz Institute Ulm, Ulm 89081, Germany*

Aleksandra Govedarica − *Department of Chemical and Petroleum Engineering, University of Calgary, Calgary, AB T2N 1N4, Canada;* ◉ orcid.org/0000-0002-2282-9018

Gabriele Kloker − *Helmholtz Institute Ulm, Ulm 89081, Germany*

Maximilian Fichtner − *Helmholtz Institute Ulm, Ulm 89081, Germany*

Vladimir K. Michaelis − *Faculty of Science − Chemistry, University of Alberta, Edmonton, AB T6G 2G2, Canada;* ◉ orcid.org/0000-0002-6708-7660

Guy M. Bernard − *Faculty of Science − Chemistry, University of Alberta, Edmonton, AB T6G 2G2, Canada*

Philipp M. Veelken − *Institute of Energy and Climate Research, IEK9, Forschungszentrum Juelich, Juelich 52425, Germany; Institute of Physical Chemistry, RWTH Aachen University, Aachen 52074, Germany*

Florian Hausen − *Institute of Energy and Climate Research, IEK9, Forschungszentrum Juelich, Juelich 52425, Germany; Institute of Physical Chemistry, RWTH Aachen University, Aachen 52074, Germany;* ◉ orcid.org/0000-0001-5712-6761

■ REFERENCES

(1) Tarascon, J.-M.; Armand, M. Nature Lithium Battery. *Nature* **2001**, *414*, 359−367.

(2) Mauger, A.; Julien, C. M.; Paolella, A.; Armand, M.; Zaghib, K. Building Better Batteries in the Solid State: A Review. *Materials (Basel)* **2019**, *12*, 3892.

(3) Zhang, X.; Wang, A.; Liu, X.; Luo, J. Dendrites in Lithium Metal Anodes: Suppression, Regulation, and Elimination. *Acc. Chem. Res.* **2019**, *52*, 3223−3232.

(4) Wang, D.; Zhang, W.; Zheng, W.; Cui, X.; Rojo, T.; Zhang, Q. Towards High-Safe Lithium Metal Anodes: Suppressing Lithium Dendrites via Tuning Surface Energy. *Adv. Sci.* **2017**, *4*, 1600168.

(5) Li, S.; Zhang, S. Q.; Shen, L.; Liu, Q.; Ma, J. B.; Lv, W.; He, Y. B.; Yang, Q. H. Progress and Perspective of Ceramic/Polymer Composite Solid Electrolytes for Lithium Batteries. *Adv. Sci.* **2020**, *7*, 1903088.

(6) Arya, A.; Sharma, A. L. Polymer Electrolytes for Lithium Ion Batteries: A Critical Study. *Ionics* **2017**, *23*, 497.

(7) Aziz, S. B.; Woo, T. J.; Kadir, M. F. Z.; Ahmed, H. M. A Conceptual Review on Polymer Electrolytes and Ion Transport Models. *J. Sci.: Adv. Mater. Devices* **2018**, *3*, 1−17.

(8) Bocharova, V.; Sokolov, A. P. Perspectives for Polymer Electrolytes: A View from Fundamentals of Ionic Conductivity. *Macromolecules* **2020**, *53*, 4141−4157.

(9) Sheng, J.; Tong, S.; He, Z.; Yang, R. Recent Developments of Cellulose Materials for Lithium-Ion Battery Separators. *Cellulose* **2017**, *24*, 4103−4122.

(10) Klemm, D.; Cranston, E. D.; Fischer, D.; Gama, M.; Kedzior, S. A.; Kralisch, D.; Kramer, F.; Kondo, T.; Lindström, T.; Nietzsche, S.; Petzold-Welcke, K.; Rauchfuß, F. Nanocellulose as a Natural Source for Groundbreaking Applications in Materials Science: Today's State. *Mater. Today* **2018**, *21*, 720−748.

(11) Thangadurai, V.; Pinzaru, D.; Narayanan, S.; Baral, A. K. Fast Solid-State Li Ion Conducting Garnet-Type Structure Metal Oxides for Energy Storage. *J. Phys. Chem. Lett.* **2015**, *6*, 292−299.

(12) Afyon, S.; Krumeich, F.; Rupp, J. L. M. A Shortcut to Garnet-Type Fast Li-Ion Conductors for All-Solid State Batteries. *J. Mater. Chem. A* **2015**, *3*, 18636−18648.

(13) Kotobuki, M.; Munakata, H.; Kanamura, K.; Sato, Y.; Yoshida, T. Compatibility of $Li_7La_3Zr_3O_{12}$ Solid Electrolyte to All-Solid-State Battery Using Li Metal Anode. *J. Electrochem. Soc.* **2010**, *157*, A1076.

(14) Pervez, S. A.; Ganjeh-Anzabi, P.; Farooq, U.; Trifkovic, M.; Roberts, E. P. L.; Thangadurai, V. Fabrication of a Dendrite-Free all Solid-State Li Metal Battery via Polymer Composite/Garnet/Polymer Composite Layered Electrolyte. *Adv. Mater. Interfaces* **2019**, *6*, 1−10.

(15) Wright, P. V. Electrical Conductivity in Ionic Complexes of Poly(Ethylene Oxide). *Br. Polym. J.* **1975**, *7*, 319−327.

(16) Ito, Y.; Kanehori, K.; Miyauchi, K.; Kudo, T. Ionic Conductivity of Electrolytes Formed from $PEO-LiCF_3SO_3$ Complex Low Molecular Weight Poly(Ethylene Glycol). *J. Mater. Sci.* **1987**, *22*, 1845−1849.

(17) Xue, Z.; He, D.; Xie, X. Poly(Ethylene Oxide)-Based Electrolytes for Lithium-Ion Batteries. *J. Mater. Chem. A* **2015**, *3*, 19218−19253.

(18) Watanabe, M.; Nagano, S.; Sanui, K.; Ogata, N. Ionic Conductivity of Network Polymers From Poly(Ethylene Oxide) Containing Lithium Perchlorate. *Polym. J.* **1986**, *18*, 809−817.

(19) Bresser, D.; Lyonnard, S.; Iojoiu, C.; Picard, L.; Passerini, S. Decoupling Segmental Relaxation and Ionic Conductivity for Lithium-Ion Polymer Electrolytes. *Mol. Syst. Des. Eng.* **2019**, *4*, 779−792.

(20) Olmedo-Martínez, J. L.; Meabe, L.; Basterretxea, A.; Mecerreyes, D.; Müller, A. J. Effect of Chemical Structure and Salt Concentration on the Crystallization and Ionic Conductivity of Aliphatic Polyethers. *Polymers (Basel)* **2019**, *11*, 452.

(21) Fu, X.; Li, Y.; Liao, C.; Gong, W.; Yang, M.; Li, R. K. Y.; Tjong, S. C.; Lu, Z. Enhanced Electrochemical Performance of Solid PEO/ $LiClO_4$ electrolytes with a 3D porous $Li_{6.28}La_3Zr_2Al_{0.24}O_{12}$ Network. *Compos. Sci. Technol.* **2019**, *184*, No. 107863.

(22) Angulakshmi, N.; Dhanalakshmi, R. B.; Kathiresan, M.; Zhou, Y.; Stephan, A. M. The Suppression of Lithium Dendrites by a Triazine-Based Porous Organic Polymer-Laden PEO-Based Electro-lyte and its Application for All-Solid-State Lithium Batteries. *Mater. Chem. Front.* **2020**, *4*, 933−940.

(23) Quartarone, E.; Mustarelli, P.; Magistris, A. PEO-Based Composite Polymer Electrolytes. *Solid State Ionics* **1998**, *110*, 1−14.

(24) Yao, P.; Yu, H.; Ding, Z.; Liu, Y.; Lu, J.; Lavorgna, M.; Wu, J.; Liu, X. Review on Polymer-Based Composite Electrolytes for Lithium Batteries. *Front. Chem.* **2019**, *7*, 1−17.

(25) Wang, W.; Fang, Z.; Zhao, M.; Peng, Y.; Zhang, J.; Guan, S. Solid Polymer Electrolytes Based on the Composite of PEO−LiFSi And Organic Ionic Plastic Crystal. *Chem. Phys. Lett.* **2020**, *747*, No. 137335.

(26) Liu, J.; Fang, W.; Gao, S.; Chen, Y.; Chen, S.; Hu, C.; Cai, S.; Liu, Z.; Liu, X. Contactless Electric−Field Driven Z-Alignment of Ceramic Nanoparticles in Polymer Electrolyte to Enhance Ionic Conductivity. *Mater. Des.* **2020**, *192*, No. 108753.

(27) Tian, H.; Le, T. H.; Yang, Y. A Fibrotic Poly (Ethylene Oxide) Polymer Electrolyte with High Ionic Conductivity for Stable Lithium Metal Batteries. *J. Mater. Sci.: Mater. Electron.* **2019**, *30*, 5038−5043.

(28) Kim, S. H.; Choi, K. H.; Cho, S. J.; Kil, E. H.; Lee, S. Y. Mechanically Compliant and Lithium Dendrite Growth-Suppressing Composite Polymer Electrolytes for Flexible Lithium-Ion Batteries. *J. Mater. Chem. A* **2013**, *1*, 4949−4955.

(29) Wang, C.; Yang, Y.; Liu, X.; Zhong, H.; Xu, H.; Xu, Z.; Shao, H.; Ding, F. Suppression of Lithium Dendrite Formation by Using LAGP-PEO (LiTFSI) Composite Solid Electrolyte and Lithium Metal Anode Modified by PEO (LiTFSI) in All-Solid-State Lithium Batteries. *ACS Appl. Mater. Interfaces* **2017**, *9*, 13694−13702.

(30) Bashiri, P.; Rao, T. P.; Naik, V. M.; Nazri, G. A.; Naik, R. AC Conductivity Studies of Polyethylene Oxide-Garnet-Type $Li_7La_3Zr_2O_{12}$ Hybrid Composite Solid Polymer Electrolyte Films. *Solid State Ionics* **2019**, *343*, No. 115089.

(31) Strawhecker, K. E.; Manias, E. Crystallization Behavior of Poly(Ethylene Oxide) in the Presence of Na^+ Montmorillonite Fillers. *Chem. Mater.* **2003**, *15*, 844−849.

(32) Syzdek, J.; Armand, M.; Marcinek, M.; Zalewska, A.; Żukowska, G.; Wieczorek, W. Detailed Studies on the Fillers Modification and Their Influence on Composite, Poly(Oxyethylene)-Based Polymeric Electrolytes. *Electrochim. Acta* **2010**, *55*, 1314−1322.

(33) Vogel, M.; Herbers, C.; Koch, B. Effects of Salt and Nanoparticles on the Segmental Motion of Polyethylene Oxide in its Crystalline and Amorphous Phases: ^2H and ^7Li NMR studies. *J. Phys. Chem. B* **2008**, *112*, 11217−11226.

(34) Best, A. S.; Adebahr, J.; Jacobsson, P.; MacFarlane, D. R.; Forsyth, M. Microscopic Interactions in Nanocomposite Electrolytes. *Macromolecules* **2001**, *34*, 4549−4555.

(35) Lin, D.; Yuen, P. Y.; Liu, Y.; Liu, W.; Liu, N.; Dauskardt, R. H.; Cui, Y. A Silica-Aerogel-Reinforced Composite Polymer Electrolyte with High Ionic Conductivity and High Modulus. *Adv. Mater.* **2018**, *30*, 1802661.

(36) Elmore, C. T.; Seidler, M. E.; Ford, H. O.; Merrill, L. C.; Upadhyay, S. P.; Schneider, W. F.; Schaefer, J. L. Ion Transport in Solvent-Free, Crosslinked, Single-Ion Conducting Polymer Electro-lytes for Post-Lithium Ion Batteries. *Batteries* **2018**, *4*, 28.

(37) Liu, M.; Wang, Y.; Li, M.; Li, G.; Li, B.; Zhang, S.; Ming, H.; Qiu, J.; Chen, J.; Zhao, P. A New Composite Gel Polymer Electrolyte Based on Matrix of PEGDA With High Ionic Conductivity for Lithium-Ion Batteries. *Electrochim. Acta* **2020**, *354*, No. 136622.

(38) Lalia, B. S.; Samad, Y. A.; Hashaikeh, R. Nanocrystalline Cellulose-Reinforced Composite Mats for Lithium-Ion Batteries: Electrochemical and Thermomechanical Performance. *J. Solid State Electrochem.* **2013**, *17*, 575−581.

(39) Xu, X.; Liu, F.; Jiang, L.; Zhu, J. Y.; Haagenson, D.; Wiesenborn, D. P. Cellulose Nanocrystals vs. Cellulose Nanofibrils: A Comparative Study on Their Microstructures and Effects as Polymer Reinforcing Agents. *ACS Appl. Mater. Interfaces* **2013**, *5*, 2999−3009.

(40) Wu, H.; Wang, J.; Zhao, Y.; Zhang, X.; Xu, L.; Liu, H.; Cui, Y.; Cui, Y.; Li, C. A Branched Cellulose-Reinforced Composite Polymer Electrolyte with Upgraded Ionic Conductivity for Anode Stabilized

Solid-State Li Metal Batteries. *Sustainable Energy Fuels* **2019**, *3*, 2642−2656.

(41) Safdari, F.; Carreau, P. J.; Heuzey, M. C.; Kamal, M. R.; Sain, M. M. Enhanced Properties of Poly(Ethylene Oxide)/Cellulose Nanofiber Biocomposites. *Cellulose* **2017**, *24*, 755−767.

(42) Qin, H.; Fu, K.; Zhang, Y.; Ye, Y.; Song, M.; Kuang, Y.; Jang, S. H.; Jiang, F.; Cui, L. Flexible Nanocellulose Enhanced Li$^+$ Conducting Membrane for Solid Polymer Electrolyte. *Energy Storage Mater.* **2020**, *28*, 293−299.

(43) Moon, R. J.; Martini, A.; Nairn, J.; Simonsen, J.; Youngblood, J. Cellulose Nanomaterials Review: Structure, Properties and Nanocomposites. *Chem. Soc. Rev.* **2011**, *40*, 3941−3994.

(44) Wald, N. *Poly (Ethylene Oxide)/Cellulose-Nanocrystal Nanocomposites as Polymer Electrolyte Membranes*: PhD diss., Drexel University, 2012.

(45) Zheng, X.; Liu, K.; Yang, T.; Wei, J.; Wang, C.; Chen, M. Sandwich Composite PEO@(Er$_{0.5}$Nb$_{0.5}$)$_{0.05}$Ti$_{0.95}$O$_2$@Cellulose Electrolyte with High Cycling Stability for All-Solid-State Lithium Metal Batteries. *J. Alloys Compd.* **2021**, *877*, No. 160307.

(46) Mohamed Ali, T.; Padmanathan, N.; Selladurai, S. Structural, Conductivity, and Dielectric Characterization of PEO−PEG Blend Composite Polymer Electrolyte Dispersed with TiO$_2$ Nanoparticles. *Ionics* **2013**, *19*, 1115−1123.

(47) Vignarooban, K.; Dissanayake, M. A. K. L.; Albinsson, I.; Mellander, B.-E. Effect of TiO$_2$ Nano-Filler and EC Plasticizer on Electrical and Thermal Properties of Poly (Ethylene Oxide)(PEO) Based Solid Polymer Electrolytes. *Solid State Ionics* **2014**, *266*, 25−28.

(48) Singh, P. K.; Bhattacharya, B.; Nagarale, R. K. Effect of Nano-TiO$_2$ Dispersion on PEO Polymer Electrolyte Property. *J. Appl. Polym. Sci.* **2010**, *118*, 2976−2980.

(49) Mezzomo, L.; Lorenzi, R.; Mauri, M.; Simonutti, R.; D'Arienzo, M.; Wi, T.-U.; Ko, S.; et al. Unveiling the Role of PEO-Capped TiO$_2$ Nanofiller in Stabilizing the Anode Interface in Lithium Metal Batteries. *Nano Lett.* **2022**, *22*, 8509−8518.

(50) Banitaba, S. N.; Semnani, D.; Heydari-Soureshjani, E.; Rezaei, B.; Ensafi, A. A. Effect of Titanium Dioxide and Zinc Oxide Fillers on Morphology, Electrochemical and Mechanical Properties of the PEO-Based Nanofibers, Applicable as an Electrolyte for Lithium-Ion Batteries. *Mater. Res. Express* **2019**, *6*, No. 0850d6.

(51) Ni'mah, Y. L.; Cheng, M.-Y.; Cheng, J. H.; Rick, J.; Hwang, B.-J. Solid-State Polymer Nanocomposite Electrolyte of TiO$_2$/PEO/NaClO$_4$ for Sodium Ion Batteries. *J. Power Sources* **2015**, *278*, 375−381.

(52) Banitaba, S. N.; Semnani, D.; Rezaei, B.; Ensafi, A. A. Evaluating the Electrochemical Properties of PEO-Based Nanofibrous Electrolytes Incorporated with TiO$_2$ Nanofiller Applicable in Lithium-Ion Batteries. *Polym. Adv. Technol.* **2019**, *30*, 1234−1242.

(53) Lin, Y.-C.; Cheng, J.-H.; Venkateswarlu, M.; Wang, F.-M.; Santhanam, R.; Hwang, B. J. Transport Properties of Nano-Sized TiO$_2$-Based Composite Polymer Electrolyte Prepared by a Green Method. *J. Chin. Chem. Soc.* **2012**, *59*, 1250−1257.

(54) Pandey, A.; Telmadarreie, A.; Trifkovic, M.; Bryant, S. Cellulose Nanocrystal Stabilized Emulsions for Conformance Control and Fluid Diversion in Porous Media. In *SPE annual technical conference and exhibition*; OnePetro, 2018, *2018-Septe*, DOI: 10.2118/191609-ms.

(55) Marzantowicz, M.; Dygas, J. R.; Krok, F.; Nowiński, J. L.; Tomaszewska, A.; Florjańczyk, Z.; Zygadło-Monikowska, E. Crystalline Phases, Morphology and Conductivity of PEO:LiTFSI Electrolytes in the Eutectic Region. *J. Power Sources* **2006**, *159*, 420−430.

(56) Jackson, J. K.; De Rosa, M. E.; Winter, H. H. Molecular Weight Dependence of Relaxation Time Spectra for the Entanglement and Flow Behavior of Monodisperse Linear Flexible Polymers. *Macromolecules* **1994**, *27*, 2426−2431.

(57) Zheng, J.; Tang, M.; Hu, Y.-Y. Lithium-Ion Pathway Within Li$_7$La$_3$Zr$_2$O$_{12}$-Polyethylene Oxide Composite Electrolytes. *Angew. Chem.* **2016**, *128*, 12726−12730.

(58) Schön, N.; Gunduz, D. C.; Yu, S.; Tempel, H.; Schierholz, R.; Hausen, F. Correlative Electrochemical Strain and Scanning Electron Microscopy for Local Characterization of the Solid-state Electrolyte Li$_{1.3}$Al$_{0.3}$Ti$_{1.7}$(PO$_4$)$_3$. *Beilstein J. Nanotechnol.* **2018**, *9*, 1564−1572.

(59) Veelken, P. M.; Wirtz, M.; Schierholz, R.; Tempel, H.; Kungl, H.; Eichel, R.-A.; Hausen, F. Investigating the Interface between Ceramic Particles and Polymer Matrix in Hybrid Electrolytes by Electrochemical Strain Microscopy. *Nanomaterials* **2022**, *12*, 654.

(60) Wu, B.; Wang, S.; Lochala, J.; Desrochers, D.; Liu, B.; Zhang, W.; Yang, J.; Xiao, J. The Role of the Solid Electrolyte Interphase Layer in Preventing Li Dendrite Growth in Solid-State Batteries. *Energy Environ. Sci.* **2018**, *11*, 1803−1810.

(61) Ren, Y.; Shen, Y.; Lin, Y.; Nan, C. W. Direct Observation of Lithium Dendrites Inside Garnet-Type Lithium-Ion Solid Electrolyte. *Electrochem. Commun.* **2015**, *57*, 27−30.